Sze *et al.*
European Journal of Medical Research (2025) 30:67
https://doi.org/10.1186/s40001-025-02305-z

European Journal of Medical Research

RESEARCH

Open Access

Comparative analysis of ocular biometrics using spectral domain optical coherence tomography with Purkinje image and optic nerve head alignments in mice

Ying Hon Sze[1,2], Bing Zuo[1], Da Qian Lu[1], King Kit Li[1], Dennis Yan Yin Tse[1,2,3], Qian Zhao[4] and Thomas Chuen Lam[1,2,3,5*]

Abstract

Background Mice are an emerging model for experimental myopia. Due to their small eye size, non-invasive optical coherence tomography is essential for evaluating ocular biometrics. There is currently no universally accepted protocol for those measurements. This study aims to compare ocular biometric measurements using two methods: Purkinje image-based alignment and optic nerve head alignment, utilizing spectral domain optical coherence tomography. Gaining an understanding of the implications of these methods in determining axial elongation in the normal growing eyes of wild-type C57BL/6J mice would offer valuable insight into their relevance for the experimental myopia model.

Methods Ocular dimensions and refractive development were measured on postnatal days P21 (n = 10), P28 (n = 15), and P35 (n = 8). The Purkinje image-based alignment (P1) was determined using a photorefractor and aligned perpendicular to the corneal apex using SD-OCT. In comparison, due to the absence of a fovea in the mouse retina, the optic nerve head (ONH) alignment was used. Variance analysis, regression analysis, and Bland–Altman analysis were performed to compare the differences between alignment methods as well as the replication by another operator.

Results Mice developed hyperopic ametropia under normal visual conditions. The photorefractor measured a technical variation of 3.9 D (95% CI, n = 170, triplicates). Bland–Altman analysis revealed a shorter (mean ± SD) axial length (− 26.4 ± 18.1 µm) and vitreous chamber depth (− 39.9 ± 25.4 µm) in the Purkinje image-based alignment. There was a significant difference in the relative growth trend in VCD (linear regression, p = 0.02), which was relatively stable and showed shortening when measured with ONH alignment from postnatal age 21 to 35 days.

Conclusions SD-OCT allowed precise *in-vivo* measurement and segmentation of ocular dimensions, regardless of the methods adopted. P1 alignment consistently resulted in significantly shorter VCD and AL compared to ONH alignment at most time points. When considering temporal changes from P21 to P35, both methods showed similar results, with significant elongation of ACD, LT, and AL as expected. However, our findings revealed a significant shortening of VCD over time with the adoption of ONH alignment, while the change in P1 alignment was relatively stable. Therefore, AL provides a better measure for evaluating ocular growth in mice using optical coherence tomography than VCD for myopia research.

*Correspondence:
Thomas Chuen Lam
thomas.c.lam@polyu.edu.hk
Full list of author information is available at the end of the article

Background

Myopia is the leading cause of distance refractive error, in which objects form in front of the retina rather than on the retina itself during emmetropization. The prevalence of myopia in Asian school children aged 6 to 19 years (60%) is significantly higher than that in Europe (40%) [1]. Much research has been performed to determine the risk factors and mechanisms of myopia development, including the use of animal models. The C57BL/6J wild-type mouse, a common inbred strain of laboratory mice, is an emerging model for experimental myopia [2], including lens-induced myopia (LIM) [3], form-deprived myopia (FDM) [4], lid suture [5], and light conditions [6], as summarized in a recently published review [7].

In experimental myopia research, ocular segmentation and refractive error measurements are relatively challenging in mice compared to chicks (*Gallus gallus*) and guinea pigs (*Cavia porcellus*). Mice have poor vision due to their small eyes, restricted cone photoreceptor population, and adaptation to a dim-light habitat, which are accompanied by reduced cone b-wave amplitude, speed, and oscillatory potentials in ERG measurements due to circadian rhythm [8]. Despite the challenges, the murine models have several advantages over traditional myopia avian models, including transgenic features, a mature and validated genome for signaling pathway analysis and the structural similarity of the mouse retina to that of humans, except that it lacks a fovea, making it useful for investigation of retinal diseases [9]. For example, the antagonizing effect of dopamine D2 receptor (D2R) was shown to be diminished in D2R-knockout mice [10], Opn5 knockout mice were used in a study of violet light suppression of myopia [11], and red light (585–660 nm) was shown to induce a significant hyperopic shift in mice [12]. The visual acuity of C57BL/6J mice has been estimated at 1.4 cycles/degree (cpd), while mammals exhibit substantial variation in visual acuity up to the highly acute vision (30–64 cpd) of diurnal anthropoid primates [13]. In comparison to other common inbred murine strains, DBA/2J and 129S1/SvlmJ and albino (AKR/J) were reported to have normal vision, whereas other albino strains (A/J, BALB/cByJ, and BALB/CJ) took longer to learn the water maze task due to poor vision. [14]

In this comparative study, spectral domain optical coherence tomography (SD-OCT), a noninvasive, in vivo high-resolution imaging technique, was used to compare the reliable micrometer ocular dimension measured with two alignment methods by Purkinje image-based (P1) and optic nerve head (ONH). The development of refractive error and technical variation in using the infrared photorefractor to capture the Purkinje image of the corneal apex. Tkatchenko et al. reported that the susceptibility of mice to experimentally induced myopia declined with age, leveling off at postnatal day 67 [15]. Therefore, experimental myopia studies in mice typically commence at postnatal day 21, after weaning, or at a later stage, P28 [16, 17]. Hence, we studied the ocular characteristics of normally growing eyes of wild-type C57BL/6J mice between P21 and P35. Comparison of the two alignment methods for ocular dimensions measured using SD-OCT and refractive error measurement with an infrared photorefractor.

Methods

Animals

Black C57BL/6J wild-type mice were imported from The Jackson Laboratory (Farmington, CT, USA), similar to our previous work [18]. Mice were maintained as in-house breeding colonies at the centralized animal facility of The Hong Kong Polytechnic University. Animals were housed in standard mouse cages (Sealsafe Plus GM500, Tecniplast, Varese, Italy) at 25 °C with a 12:12 h light/dark cycle in a room of 150 lx with food and water available ad libitum. Mice were weaned on postnatal day 21 and housed until postnatal day 35. Researchers were licensed by the Department of Health, HKSAR government, and all procedures performed in this study received ethics approval from the Animal Subjects Ethics Sub-Committee (ASESC), The Hong Kong Polytechnic University, and complied with the Association of Research in Vision and Ophthalmology (ARVO) statement for the use of animals in ophthalmology and vision research.

Refractive error measurement using an eccentric infrared photorefractor

The eccentric infrared photorefractor was developed by Prof. Frank Schaeffel (Steinbeiss-Transfer Centre for Biomedical Optics, Tuebingen, Germany) and used according to the user manual [19]. To prepare the mice for the measurements, a drop of mydrin-P ophthalmic solution [3] containing 0.5% tropicamide and 0.5% phenylephrine hydrochloride was administered to dilate the pupils. After 15 min, mice were sedated through intraperitoneal injection with a mixture of ketamine (70 mg/kg) and xylazine (10 mg/kg). Subsequently, they were carefully positioned on the cylindrical platform of the spectral domain optical coherence tomography (SD-OCT). All biometric measurements were conducted while the mice were under anesthesia. The refractive errors were acquired by aligning the measurement to the Purkinje image obtained from the corneal reflection, known as P1. The alignment was performed using software-controlled gaze control, with adjustments made to ensure the alignment was within 5 degrees in the x- and y-axes. In addition, each

measurement was carefully adjusted to approach zero in the x- and y-axes, collecting 99 data points per eye. The refractive error measurements were recorded as the mean value ± SD in diopters (D), and each measurement was repeated in triplicate. To assess instrument variability, the standard deviation of the technical replicate was calculated for each eye of C57BL/6J mice at postnatal day 21 (n = 170, eyes = 340, triplicates), an early time point for optical-based experimental myopia. A Python script was developed to facilitate the analysis of a large dataset.

Two alignment methods for spectral domain optical coherence tomography

First, mice were measured with the Purkinje image-based alignment method (P1). The photorefractor was positioned behind the SD-OCT probe holder, ensuring that they shared the same axis of measurement. Upon acquiring refractive error data using the photorefractor, the ocular segmentation was immediately measured using SD-OCT. The ocular structure could be observed by adjusting the distance of the probe, horizontal and vertical position adjustments on the OCT platform without further angular movement until it was perpendicular to the corneal apex. The retinal fundus image indicated a nasal position relative to the optic disc. The probe was returned to the optimal distance determined by perpendicular alignment to the corneal apex while maintaining a live view of the entire eye. Followed by measurement with the optic nerve head (ONH) alignment method. Mouse were positioned to the Purkinje image using an infrared photorefractor. The retinal fundus image was achieved by positioning the OCT probe near the eyeball until a clear retinal fundus image was visualized in the live view window. To facilitate this alignment, the digital single-point centered crosshair was set to a diameter of 0.4 mm. The mouse eye position was then adjusted to approximately 0.2 mm above the optic disc, using the radius of the crosshair as a reference in the software. The mouse position was rotated until a match was achieved. To obtain the length of the entire eye, the SD-OCT probe was returned to the optimal distance determined by perpendicular alignment to the corneal apex and a live view of the whole eye. It is important to note that misalignment between the photorefractor and the ONH position in SD-OCT measurements necessitated re-positioning of the mice after the refractive error measurement. This re-positioning did not provide control over the angle of measurement and relied solely on the retinal fundus position. The differences between the alignment methods and their corresponding retinal positions are visually presented in Fig. 1.

Ocular biometric measurements using spectral domain optical coherence tomography

The eye was scanned using radial volume mode in duplicate (A-scans = 1000 lines, B-scans = 6, 32 frames, 80 lines of inactive A-scans, 0.4 mm diameter). The length of each component was reported as the mean ± SD in micrometers. The segmented ocular dimensions were measured using spectral domain-optical coherence tomography (SD-OCT, Envisu R4310, Leica, Germany) equipped with a 50° probe for mice [20]. After each SD-OCT measurement, the mice were reset to the default position and acquired in duplicate. The ocular segmentation was analyzed manually using the digital caliper in the OCT data analysis software (InVivoVue, ver. 2.4, Leica). The distances were determined by identifying the intersections between the boundaries of each ocular compartment and the reflected light array from the mice eyes. Axial length (AL) was represented as the sum of all ocular segments, including corneal thickness (CT) measured from the anterior corneal surface to the posterior corneal surface. The anterior chamber depth (ACD) is the distance from the posterior cornea surface to the anterior lens surface. Lens thickness (LT) is the distance from the anterior lens surface to the posterior lens surface. Vitreous chamber depth (VCD) is the distance from the posterior lens surface to the retinal nerve fiber layer. Lastly, retinal thickness (RT) is the depth of the retinal nerve fiber layer up to the retinal pigment epithelium. (Supplementary Fig. 1).

Results

Validation of instrumental variation in photorefractor and optical coherence tomography

The precision and reproducibility of refractive error measurement were demonstrated by the 95th percentile of the standard deviation (SD) of technical replicates at ± 3.9 D. The mean technical variation was 1.4 ± 1.2 D, with a median of 1.1 D. The mean refractive error (mean ± SD) was determined to be 1.3 ± 6.5 D (n = 170, eyes = 340, triplicates) in mice aged P21. (Fig. 2a) The instrumental variation of SD-OCT measured with two alignment methods (n = 33, eyes = 66, duplicates) was demonstrated in the coefficient of variation (CV) and was similar between alignment methods in all ocular components. The axial length (AL) exhibited the least variation, with mean ± SD values of 1.17 ± 0.24% (P1) and 1.16 ± 0.14% for the ONH alignment. In contrast, the highest variation in retinal thickness had CV values of 9.97 ± 5.04% (P1) and 9.62 ± 2.97% (ONH). The higher variation in retinal thickness may be attributed to the limited resolution of the retinal pigment epithelium and choroidal sclera boundary. The ONH alignment method

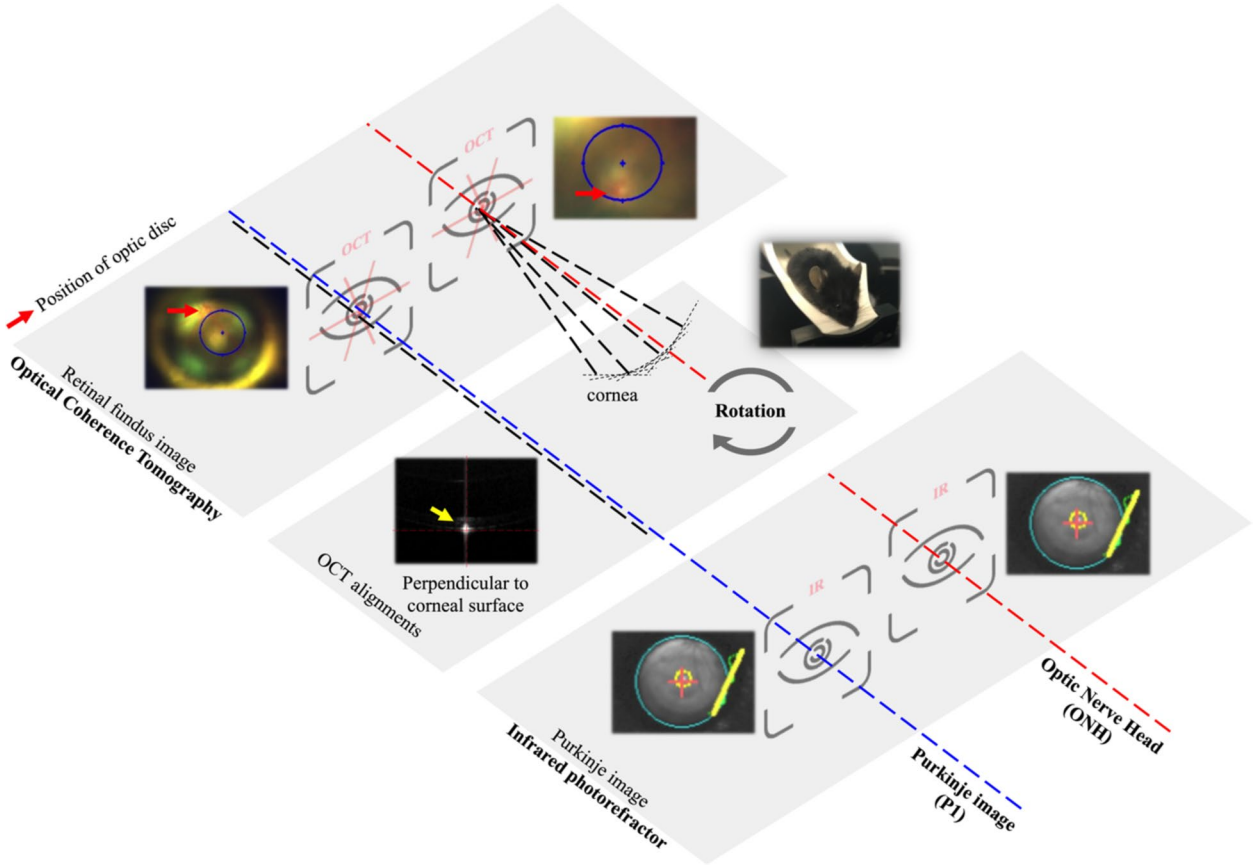

Fig. 1 Schematic illustration of SD-OCT and infrared photorefractor measurements with two alignment methods. For the Purkinje image-based alignment (P1, blue dotted line), mouse eyes were aligned to the Purkinje image-based P1. Subsequently, using SD-OCT, the eyes were aligned perpendicular to the corneal apex, ensuring consistent axis measurements between the instruments. The retinal fundus image indicated a nasal position relative to the optic disc. In comparison, the optic nerve head alignment (ONH, red dotted line), involved a standalone SD-OCT operation. The alignment was achieved by positioning the probe 0.2 mm above the optic disc, guided by a digital single-point centered crosshair with a diameter of 0.4 mm (blue circle). It is important to note that this alignment method required the rotation of mice after refractive error measurement, resulting in a lack of control over the angle of measurement (black dotted line). The retinal image captured from SD-OCT near the optic nerve head (red arrow) highlights the differences between alignment methods and their corresponding retinal positions

has slightly better performance in VCD (P1: 3.51 ± 1.28%; ONH: 2.19 ± 0.33%). Conversely, P1 alignment performed better when interpreting CT (P1: 3.32 ± 0.90%; ONH: 4.36 ± 2.38%). Overall, ocular segmentation showed variation of less than 5% CV except for retinal thickness, indicating relatively consistent results between alignment methods. The comparable magnitude of CV values obtained with the two alignment methods in all ocular segmentations may suggest a systematic variation in measuring ocular dimensions using SD-OCT in mice.

Comparison of intraocular biometrics with two alignment methods by SD-OCT

Mouse eyes, specifically the right eye (OD) and left eye (OS), were measured using SD-OCT with two alignment methods. The normal growing C57BL/6J mouse eyes showed no statistically significant interocular differences in any of the ocular segments on P21 (n = 10), P28 (n = 15), or P35 (n = 8) analyzed with two-way ANOVA and Bonferroni correction when measured in Purkinje image-based alignment (Fig. 3a, Table 1a) and 0.2 mm above the optic disc (Fig. 3b, Table 1b). Notably, both alignments revealed a similar observation of significant elongation in the anterior segments of the eye, including CT, ACD, and LT from P21 to P35. However, there were no statistically significant differences in VCD, regardless of the alignment method. There was a minor, inconsistent observation of retinal thickness between alignment methods. In the Purkinje image-based alignment, a significantly shorter retinal thickness was observed between P21 and P35 ($p < 0.05$) in the OD eye, whereas a significantly shorter retinal thickness was determined between P21 and P28 ($p < 0.05$). Overall, the results confirm no significant interocular differences in the ocular segments

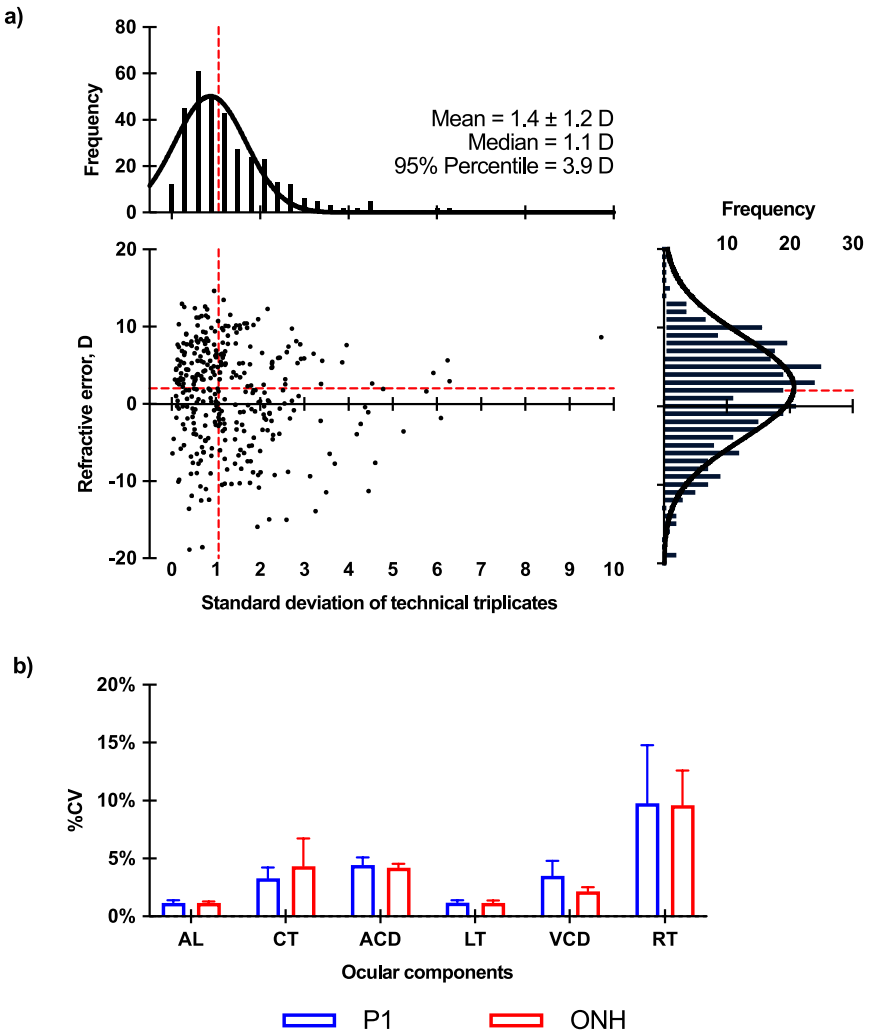

Fig. 2 Distribution and variation of refractive error and ocular biometrics using infrared photorefractor and optical coherence tomography. **a** Scatter plot of refractive error and standard deviation measured by the photorefractor. The distribution and technical standard deviation followed a normal distribution, with a 95% percentile value of 3.9 D. At postnatal age 21, the mean refractive error was 1.3 ± 6.5 D, while the mean standard deviation was 1.4 ± 1.2 D (n = 170, eyes = 340, triplicates). **b** Coefficient of variation (CV) analysis (n = 33, eyes = 66, duplicates) of ocular biometrics measured by SD-OCT between alignment methods, with the least variation in axial length (1.2%) and the highest variation in retinal thickness (9.7%). Median values of each frequency distribution (red lines). Axial length (AL), corneal thickness (CT), anterior chamber depth (ACD), lens thickness (LT), vitreous chamber depth (VCD), and retinal thickness (RT)

between the OD and OS eyes, regardless of the alignment method.

Comparative analysis of ocular biometrics in two alignment methods by SD-OCT

The OD and OS eyes of mice were not significantly different when analyzed with a two-way ANOVA and Bonferroni correction, as mentioned in the previous section. The ocular biometrics on P21 (n = 10, eyes = 20), P28 (n = 15, eyes = 30), and P35 (n = 8, eyes = 16) were consolidated based on the alignment methods, regardless of specific eyes. Interestingly, no statistically significant differences were observed in the anterior eye segments, including corneal thickness (CT), anterior chamber depth (ACD), and lens thickness (LT). However, there was a significantly shorter axial length presented in the mean ± standard error (SE) of − 33.2 ± 12.3 μm measured with P1 alignment at P21 (P1: 3011.5 ± 40.5 μm; ONH: 3044.7 ± 37.2 μm, p = 0.03). The difference persisted with a shorter axial length (mean ± SD: − 22.3 ± 7.6 μm) at P28 (P1: 3138.8 ± 27.8 μm; ONH: 3161 ± 31.3 μm, p = 0.02). Intriguingly, there was a significantly thicker retinal thickness (mean ± SE: 18.7 ± 5.3 μm) at P21 only (P1: 212.8 ± 12.9 μm; ONH:

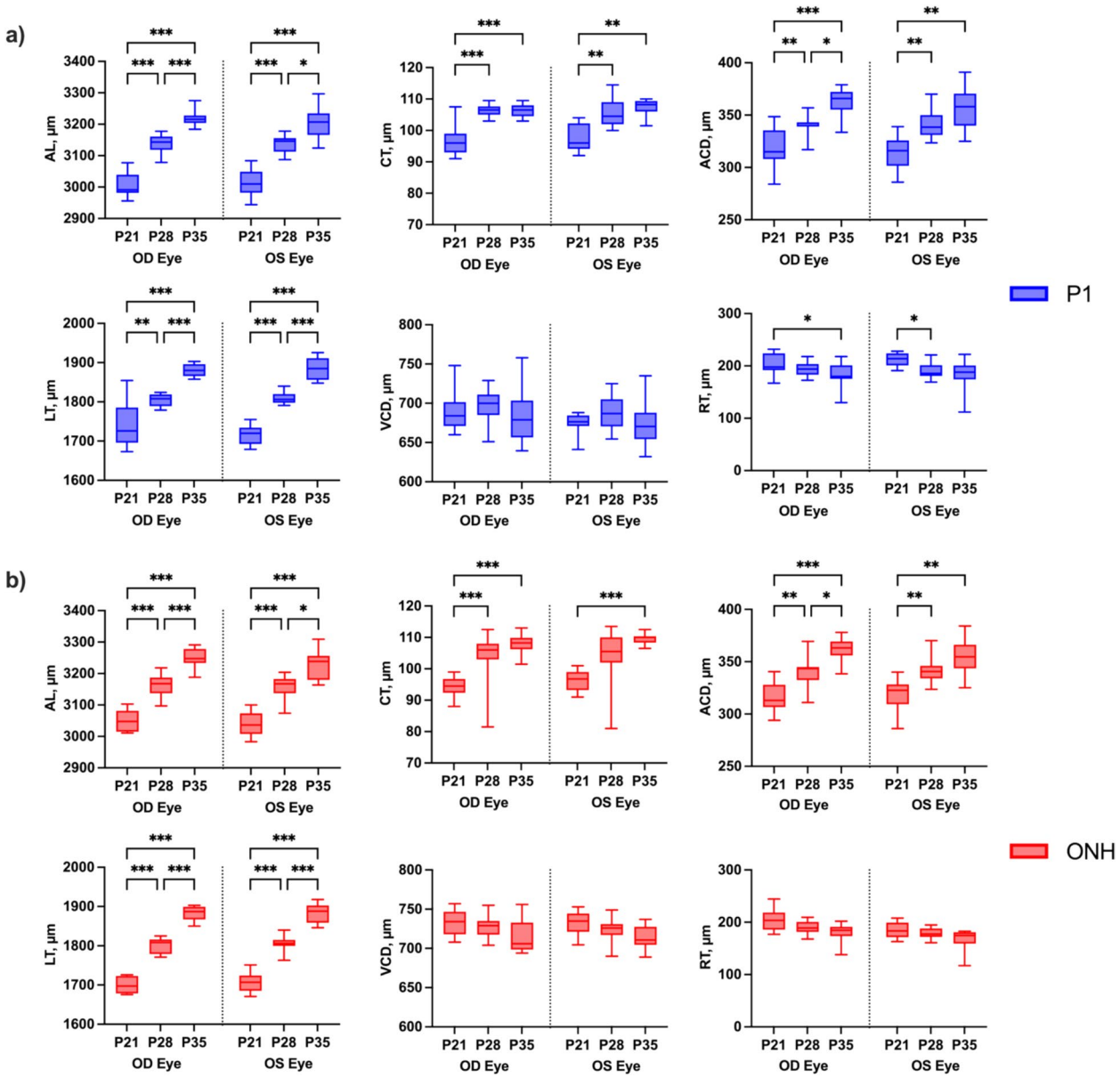

Fig. 3 Comparison of interocular biometrics measured by SD-OCT with two alignment methods. Box plot of axial length, corneal thickness, anterior chamber depth, lens thickness, and retinal thickness on P21 (n = 10), P28 (n = 15), and P35 (n = 8). **a** Purkinje image-based alignment (P1). **b** Optic nerve head (ONH). SD-OCT measurements were acquired in duplicate. Statistical analysis was performed using a two-way ANOVA with Bonferroni correction. The statistical significance levels are presented as $p \leq 0.001$ (***), $p \leq 0.01$ (**), and $p \leq 0.05$ (*). Axial length (AL), corneal thickness (CT), anterior chamber depth (ACD), lens thickness (LT), vitreous chamber depth (VCD), and retinal thickness (RT)

194.1 ± 20.1 µm, p = 0.001). Furthermore, a consistent observation of shorter vitreous chamber depth (VCD) when measured with Purkinje image-based alignment on P21 (mean ± SE: − 55.8 ± 4.9 µm, $p < 0.001$), P28 (mean ± SE: − 32.2 ± 4.9 µm, $p < 0.001$) and P35 (mean ± SE: − 34.6 ± 9.4 µm, p = 0.004) (Fig. 4a, Table 2). There is a positive correlation between axial elongation and the growth of the anterior segment, specifically CT, ACD, and LT. The 95% confidence bands indicated that there were no significant differences in the measured growth rate between the alignment methods in the anterior segment. On average, the axial length elongation was approximately + 98 µm/week. The corneal thickness increased by 5.5 µm/week, contributing to 5.6% of the total growth of the eye. Anterior chamber depth gained 22 µm/week, a 22.4% of the total growth. Lens thickness

Table 1 (a) Ocular biometrics measured with Purkinje image-based alignment (b) Ocular biometrics measured with optic nerve head alignment

Posnatal Days	P21		P28		P35	
Eyes	OD	OS	OD	OS	OD	OS
a						
AL (μm)	3008.2 ± 38.2	3014.7 ± 44.4	3138.5 ± 28.3	3139 ± 28.3	3219.5 ± 26.7	3205.6 ± 52.5
CT (μm)	97.2 ± 4.8	97.6 ± 4.3	106.4 ± 1.9	105.5 ± 4.5	106.4 ± 2.2	107.4 ± 2.8
ACD (μm)	318.6 ± 17.7	314.2 ± 16.5	340.3 ± 10	342.4 ± 14.2	362.9 ± 14.2	357.1 ± 20.6
LT (μm)	1740 ± 53.3	1716.7 ± 24.6	1805.3 ± 16.1	1809.8 ± 13.3	1880.8 ± 16.4	1885.3 ± 28.1
VCD (μm)	687.7 ± 23.4	674.1 ± 13.8	697 ± 23.7	689.3 ± 21.6	684.9 ± 36.6	673.6 ± 30.5
RT (μm)	203.3 ± 19.6	211.9 ± 12.1	194 ± 15.1	190.6 ± 15.7	182.4 ± 25.9	182.6 ± 32.3
b						
AL (μm)	3049.8 ± 35.4	3039.6 ± 40.1	3162.5 ± 31.4	3159.6 ± 32.1	3249 ± 32.3	3228.9 ± 47.7
CT (μm)	94.4 ± 3.3	96.3 ± 3.3	104.4 ± 7.1	104.7 ± 7.9	107.9 ± 3.4	109.6 ± 1.8
ACD (μm)	316.3 ± 13.8	318.6 ± 15.9	339.5 ± 13.3	342.6 ± 14	361.8 ± 11.7	355.4 ± 17.7
LT (μm)	1700.4 ± 20.8	1707.3 ± 26.3	1800 ± 17.9	1807.5 ± 18	1882.6 ± 18.6	1884.2 ± 24.9
VCD (μm)	733.2 ± 16.7	732.6 ± 14.8	728.2 ± 14.4	724.4 ± 13.7	714.3 ± 21.9	713.4 ± 15.2
RT (μm)	203.2 ± 20.8	185 ± 15.4	189.3 ± 11.5	178.9 ± 9.6	179.9 ± 19.3	167.3 ± 22.1

Data are presented as the mean ± SD. OD = right eye; OS = left eye; ocular segmentation with axial length (AL), corneal thickness (CT), anterior chamber depth (ACD), lens thickness (LT), vitreous chamber depth (VCD), and retinal thickness (RT)

contributed significantly with a growth rate of 84.9 μm/week, accounting for 86.6% of the axial elongation. In terms of vitreous chamber depth, there was a significant difference in the slope of the linear regression ($p = 0.02$). In the Purkinje image-based alignment method, the VCD remained relatively constant with equation $y = 0.4x + 670.8$ ($r^2 = 0.0079$). However, when measured using the ONH alignment method, the VCD was shorter as mice matured, with equation $y = -1.52x + 767.6$, tested for linearity with $r^2 = 0.9922$ (Fig. 4b).

To compare the differences between alignment methods. Bland–Altman analysis comparing differences (P1 – ONH) over the average of the two alignment methods from P21 to P35 (n = 33, eyes = 66). The mean differences between the methods were examined in all ocular segmentations. The 95% confidence intervals (mean; 95% CI) indicate large differences between alignment methods in AL (− 26.4 μm; − 62 to 9.1 μm) and VCD (− 39.9 μm; − 89.9 to 9.96 μm). All other ocular segments were similar between alignment methods, including CT (0.118 μm; − 7.9 to 8.1 μm), ACD (−1.47 μm; −13.5 to 10.6 μm), LT (4.1 μm; − 15.2 to 23.4 μm), and RT (10.7 μm; − 25.8 to 47.2 μm). (Fig. 5a).

In addition, the normality test indicated that the two alignment methods sampled a Gaussian normal distribution in AL, VCD, and RT and failed the normality test in CT ($p < 0.001$), ACD ($p < 0.001$), and LT ($p < 0.001$) computed with the D'Agostino & Pearson test. (Fig. 5b) These results highlighted that the significant differences in AL and VCD between methods were represented in Gaussian mean values, sampled from a normally distributed sample. In addition, the scatter plot showing individual data points, represented as the mean ± SD, showed that the AL (−26.4 ± 18.1 μm) and VCD (−39.9 ± 25.4 μm) were shorter when measured by Purkinje image-based alignment. (Fig. 5c).

An independent replication was conducted by another operator in another batch of independent animals in duplicate (n = 8, eyes = 16), with a similar pattern as mentioned previously. There were significant differences (mean; 95% CI) in AL (−27.8 μm; − 62.5 to 6.8 μm) and VCD (− 32.4 μm; − 78.1 to 13.2 μm), while no differences were observed in other segments. (Fig. 6a) The Q–Q plot indicates a Gaussian normal distribution in AL, CT, LT, VCD, and RT, whereas the ACD failed the normality test ($p < 0.001$) computed by the D'Agostino & Pearson test. (Fig. 6b) The scatter plot shows individual data points, represented as the mean ± SD, with a significant shift in AL (− 27.8 ± 17.7 μm) and VCD (−32.4 ± 23.3 μm). These results confirmed that there are significant differences between alignment methods and those repeated in independent animals by another operator.

Discussion

This dataset demonstrated that the eccentric infrared photorefractor allows rapid collection of 99 scans per measurement by computer-controlled gaze control using the Purkinje image utilized in the Purkinje image-based alignment (P1). The 95-percentile boundary at 3.9 D (n = 170, eyes = 340, triplicates) demonstrated that the

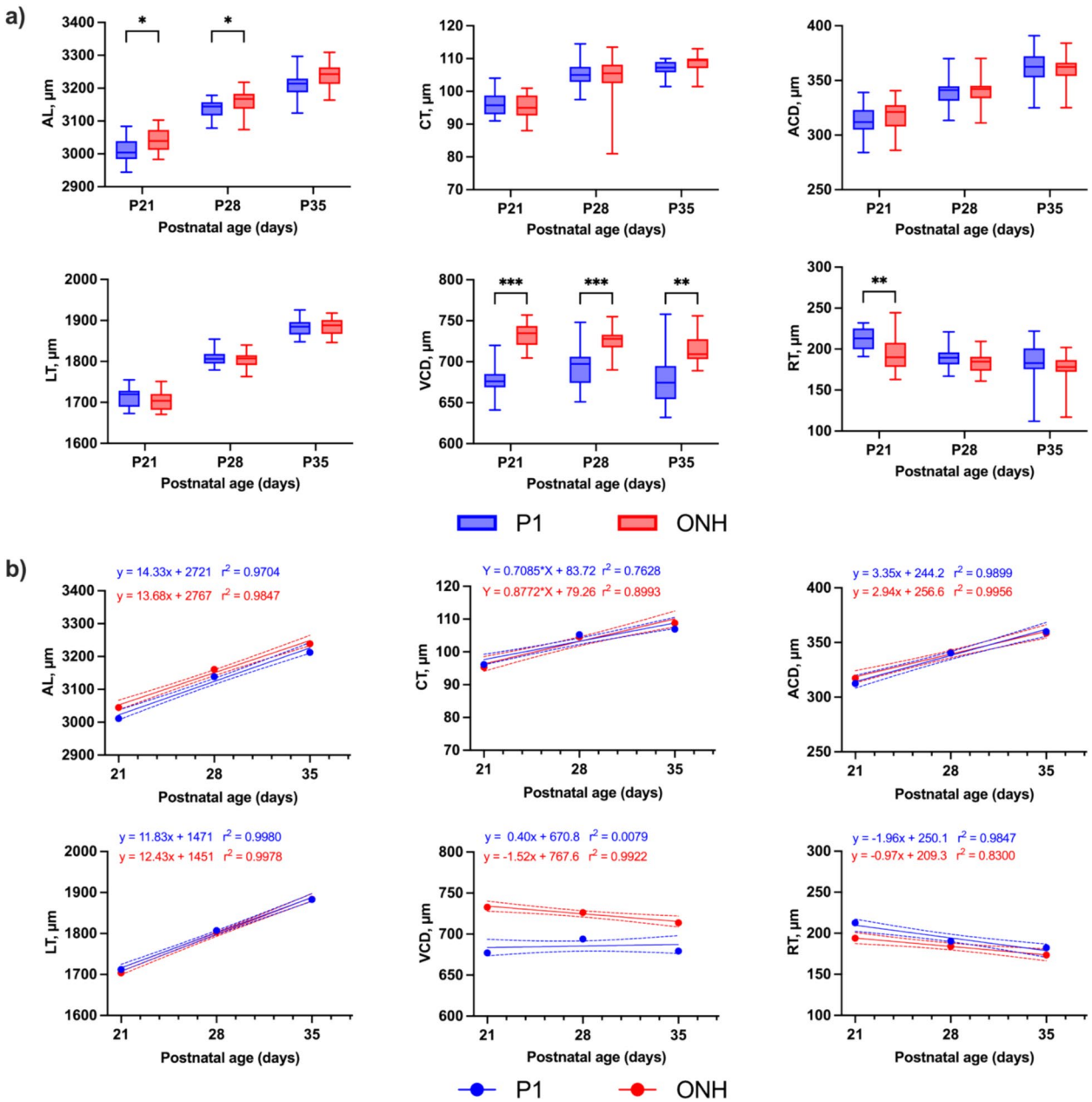

Fig. 4 Comparative analysis of ocular biometrics in two alignment methods by SD-OCT. **a** Box plots of eyes measured by P1 and ONH alignment on P21 (n = 10), P28 (n = 15), and P35 (n = 8). Significantly shorter AL on P21 and P28 and VCD from P21 to P35. Significantly longer retinal thickness was measured on P21. **b** Scatter plot with linear regressions (solid line) in ocular biometrics measured by two alignment methods and 95% confidence bands (dotted line). There were no significant differences between the slopes between the two alignment methods in AL, CT, ACD, LT, and RT. In contrast, there is a significant difference between the slopes (linear regression, p = 0.02) in VCD. SD-OCT measurements were acquired in duplicate. Statistical analysis was performed using a two-way ANOVA with Bonferroni correction. The statistical significance levels are presented as $p \le 0.001$ (***), $p \le 0.01$ (**), and $p \le 0.05$ (*). Axial length (AL), corneal thickness (CT), anterior chamber depth (ACD), lens thickness (LT), vitreous chamber depth (VCD), and retinal thickness (RT)

measurement of refractive error in early-age mice agrees with Schaeffel et al. who reported an average standard deviation of 3.0 D in C57BL/6J mice under tropicamide cycloplegia without anesthesia [2]. In this study, the refractive error of C57BL/6J mice at an early age of P21 under normal visual conditions was determined with a mean (± SD) value of 1.4 ± 1.2 D (n = 170, eyes = 340, triplicates), a generally hyperopic trend that is consistent

Table 2 Comparison of axial length and vitreous chamber depth with two alignment methods

Postnatal days	Axial length, AL (μm)			Vitreous chamber depth, VCD (μm)		
	P1	ONH	p-value	P1	ONH	p-value
P21	3011.5 ± 40.5	3044.7 ± 37.2	0.03 (*)	677.2 ± 15.8	732.9 ± 15.4	< 0.001 (***)
P28	3138.8 ± 27.8	3161 ± 31.3	0.02 (*)	694.1 ± 23.2	726.3 ± 14	< 0.001 (***)
P35	3212.5 ± 40.9	3238.9 ± 40.7	n.s	679.3 ± 33	713.8 ± 18.2	0.004 (**)

The Purkinje image-based alignment method (P1) and the optic nerve head (ONH) alignment method. SD-OCT measurements were acquired in duplicate. Statistical analysis was performed using a two-way ANOVA with Bonferroni correction. The statistical significance levels are presented as $p \leq 0.001$ (***), $p \leq 0.01$ (**), and $p \leq 0.05$ (*)

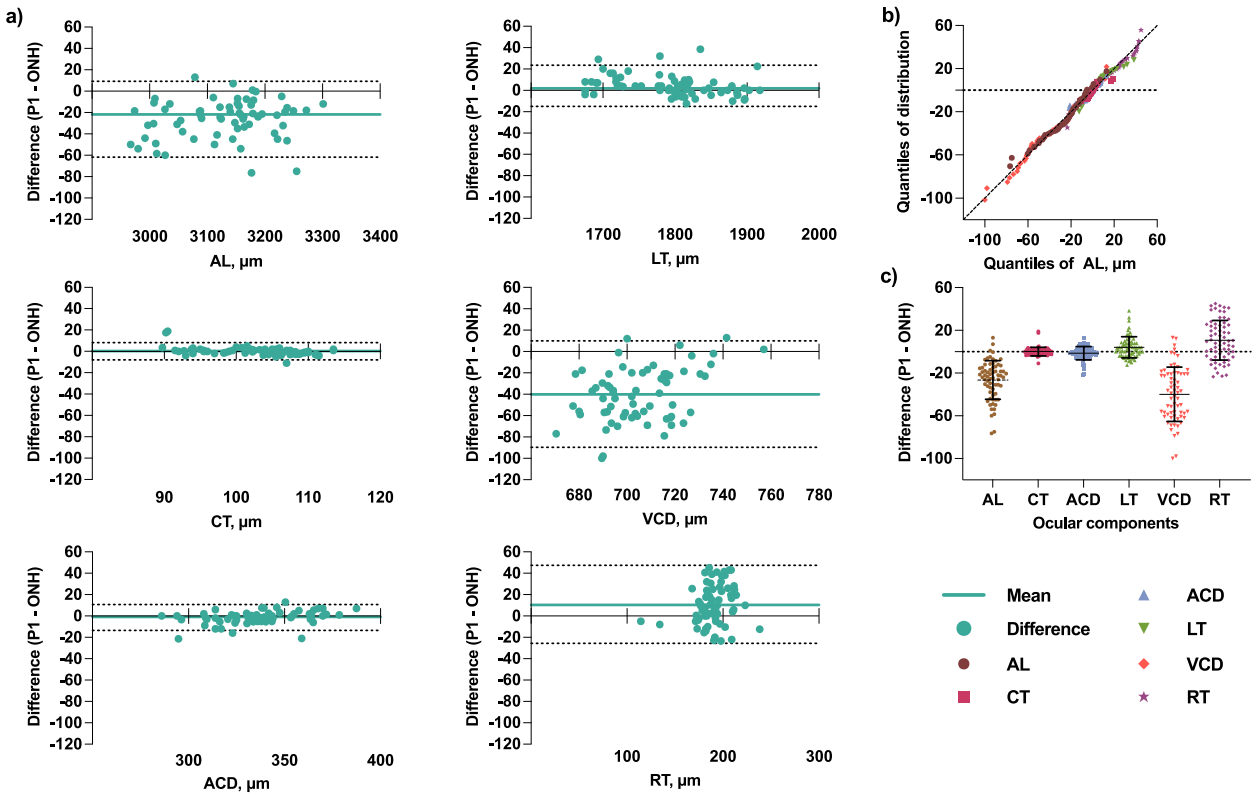

Fig. 5 Bland–Altman analysis of the ocular biometric differences in two alignment methods. **a** Bland–Altman plot comparing differences (P1 – ONH) over the average of the two alignment methods from P21 to P35 (n = 33, eyes = 66). The mean differences of methods (solid line) and 95% limits of agreement (dotted line) in AL (95% CI: – 62 to 9.1) and VCD (95% CI: – 89.8 to 9.96) are similar between alignment methods in other ocular segments. **b** Normality test on each ocular component represented in the Q–Q plot. **c)** Scatter plot of alignment method differences with mean ± SD, a significantly shorter AL (– 26.4 ± 18.1 μm, paired t test, $p < 0.0001$) and VCD (– 39.9 ± 25.4 μm, paired t test, $p < 0.0001$) when measured with Purkinje image-based alignment. SD-OCT measurements were acquired in duplicate. Axial length (AL), corneal thickness (CT), anterior chamber depth (ACD), lens thickness (LT), vitreous chamber depth (VCD), and retinal thickness (RT)

with previous reports in older mice, as summarized in a review [9]. It is worth noting that despite the hyperopic refractive error, the small eye artifacts in mice suggest that the true refraction is likely to be less hyperopic [21]. In parallel, the spectral-domain optical coherence tomography (SD-OCT) technique was employed in much experimental myopia research. This study uses SD-OCT to determine mouse eye dimensions extensively due to several advantages, such as high-resolution ocular segmentation, in vivo capture of images, and a noninvasive imaging technique that eliminates the need for sacrificing animals, which is crucial when monitoring axial elongation at multiple time points during myopia development. Unlike other techniques, such as *ex-vivo* fixation, which may result in structural deformation and shrinkage in the eyes within 5 min after execution [3]. Alternatively,

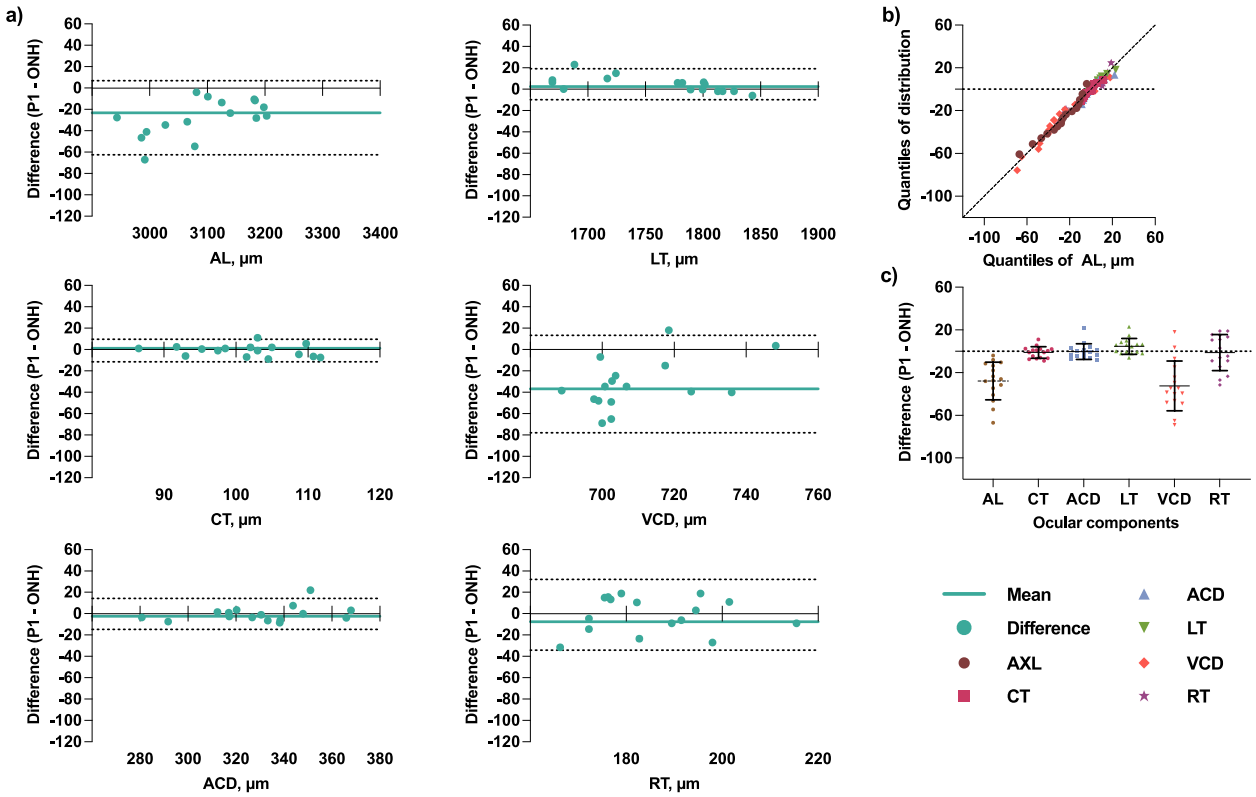

Fig. 6 Operator replicates of ocular biometric differences in two alignment methods. **a** Bland–Altman plot comparing differences (P1 – ONH) over the average of the two alignment methods (n = 8, eyes = 16, duplicates). The mean differences of methods (solid line) and 95% limits of agreement (dotted line). Mean differences between methods were observed in AL (95% CI: – 62.5 to 6.8) and VCD (95% CI: – 78.1 to 13.2). **b** Normality test on each ocular component represented in the Q–Q plot. **c** Scatter plot of method differences with mean ± SD, a significantly shorter AL (– 27.8 ± 17.7 µm, paired t test, $p < 0.0001$) and VCD (– 32.4 ± 23.3 µm, paired t test, $p < 0.0001$) when measured in Purkinje image-based alignment. SD-OCT measurements were acquired in duplicate. Axial length (AL), corneal thickness (CT), anterior chamber depth (ACD), lens thickness (LT), vitreous chamber depth (VCD), and retinal thickness (RT)

microcomputed tomography (µCT) would require an injection of contrast agent in the eye and lower ocular resolution than SD-OCT [22]. Park et al. reported similar ocular measurements with alternative in vivo imaging techniques using 780 nm partial coherence interferometry (PCI) compared to SD-OCT measurements and similar magnitudes measured with magnetic resonance imaging (MRI) techniques [23, 24].

In a murine model, Dräger et al. reported that the position of the optic disc was rather precisely in the geometric center of the retina in a whole-mount fixation study [25]. Sterratt et al. quantitatively reported that the optic disc was located colatitude at 3.7 ± 7.4° away from the geometrical center computed using 72 flat-mounted adult mouse retinas. [26] This raises one of the challenges due to the absence of the fovea aligning along the visual axis as defined in the human eye [27] and being replaced by the optic disc in mice. Therefore, the optic nerve head (ONH) alignments were found to have significantly longer VCD and AL at an early age between P21 and P35 compared to the Purkinje image-based alignment (P1), which suggests good agreement with the optical axis or visual axis of the mouse eye. This observation is in good agreement with a previous report that misalignment in the vertical meridian measurement results in the greatest change in AL but is insignificant at postnatal day 58. The shorter VCD and AL in the Purkinje image-based alignment located in the nasal retina may suggest an uneven distribution of retinal thickness superior to the ONH and the representative spherical position in the retina. In particular, a computational analysis identified mouse retinas with optic axes determined at 64° azimuth and 22° elevation [26]. In agreement with the recent report that the VCD significantly decreased and the RT significantly increased with the increasing degrees from the ONH [28]. In addition, an uneven distribution of S-opsin was observed across the dorsal, nasal, temporal, and ventral retinas in retinal flat mounts, with a denser population observed in the ventral-nasal retina [26]. The constant length of VCD from P21 to P35 (Fig. 4b) when measured

in Purkinje image-based alignment was in good agreement with observations in experimental animal models such as guinea pigs [29] and the relatively constant VCD in early age between postnatal days 21 and 42 in mice [24]. These differences between alignment methods were also supported by the fact that there were no significant intra-method differences between eyes. (Fig. 3) Most importantly, the significantly longer VCD measured in ONH alignment is clinically relevant, referring to the reported VCD elongation ranges between 38 and 50 µm in myopia research [15]. The shortening of retinal thickness measured with Purkinje image-based alignment ($y = -1.96x + 250.1$; $r^2 = 0.985$) is consistent with the reported normative retinal thickness in C57BL/6J mice, a thinning of retinal thickness on P28 (209.9 ± 3.1 µm), P56 (202.2 ± 2.9 µm), and P112 (199.2 ± 4 µm). [30]

Conclusion

SD-OCT enables precise *in-vivo* measurement of ocular segmentation. It was observed that the Purkinje image-based alignment (P1) resulted in significantly shorter axial length, primarily due to a shorter vitreous chamber depth, compared to the ONH alignment. This emphasizes the importance of understanding the alignment methods in optical-based techniques. These variations in alignment methods can potentially lead to misleading interpretations of results, particularly in myopia research that focuses on the axial length of the eye. When evaluating temporal ocular growth in mice, a significant shortening of VCD was observed when using the ONH alignment method. Therefore, axial length measurements offer better consistency than vitreous chamber depth when different alignments are employed with OCT.

Supplementary Information

The online version contains supplementary material available at https://doi.org/10.1186/s40001-025-02305-z.

Supplementary Material 1.

Author contributions

YHS, BZ, DQL conducted the experiments. YHS analyzed the results and draft the paper. DYYT, QZ and TCL provided materials, funding support and advice. YHS, ZB, KKL, DYYT, QZ and TCL edited the paper.

Funding

This study was partly funded by the InnoHK initiative, the Hong Kong Special Administrative Region Government; the Research Centre for SHARP Vision (P0043871; P0039545); General Research Fund (GRF) (15104819; 151060/18M); Research Impact Fund (R5032-18); Shenzhen Science and Technology Innovation Commission JCY20180507183409601, The Hong Kong Polytechnic University and the RGC-CRF equipment grant C5033-19E.

Availability of data and materials

The datasets used and/or analyzed during the current study available from the corresponding author on reasonable request.

Declarations

Ethics approval and consent to participate

Researchers were licensed by the Department of Health, HKSAR government, and all procedures performed in this study received ethics approval from the Animal Subjects Ethics Sub-Committee (ASESC), The Hong Kong Polytechnic University and complied with the Association of Research in Vision and Ophthalmology (ARVO) statement for the use of animals in ophthalmology and vision research.

Competing interests

The authors declare no competing interests.

Author details

[1]Centre for Myopia Research, School of Optometry, The Hong Kong Polytechnic University, Hong Kong, China. [2]Centre for Eye and Vision Research (CEVR), 17W Hong Kong Science Park, Hong Kong, China. [3]Research Centre for SHARP Vision (RCSV), The Hong Kong Polytechnic University, Hong Kong, China. [4]State Key Laboratory of Chemical Biology and Drug Discovery, Department of Applied Biology and Chemical Technology, The Hong Kong Polytechnic University, Hong Kong, China. [5]Shenzhen Research Institute, The Hong Kong Polytechnic University, Shenzhen 518052, China.

Received: 17 October 2023 Accepted: 16 January 2025
Published online: 03 February 2025

References

1. Grzybowski A, Kanclerz P, Tsubota K, Lanca C, Saw SM. A review on the epidemiology of myopia in school children worldwide. BMC Ophthalmol. 2020;20:27. https://doi.org/10.1186/s12886-019-1220-0.
2. Schaeffel F, Burkhardt E, Howland HC, Williams RW. Measurement of refractive state and deprivation myopia in two strains of mice. Optom Vis Sci. 2004;81:99–110. https://doi.org/10.1097/00006324-200402000-00008.
3. Jiang X, et al. A highly efficient murine model of experimental myopia. Sci Rep. 2018;8:2026. https://doi.org/10.1038/s41598-018-20272-w.
4. Li Q, et al. Form-deprivation myopia downregulates calcium levels in retinal horizontal cells in mice. Exp Eye Res. 2022;218: 109018. https://doi.org/10.1016/j.exer.2022.109018.
5. Barathi VA, Boopathi VG, Yap EP, Beuerman RW. Two models of experimental myopia in the mouse. Vision Res. 2008;48:904–16. https://doi.org/10.1016/j.visres.2008.01.004.
6. Zhang P, Zhu H. Light signaling and myopia development: a review. Ophthalmol Ther. 2022;11:939–57. https://doi.org/10.1007/s40123-022-00490-2.
7. Schaeffel F, Feldkaemper M. Animal models in myopia research. Clin Exp Optom. 2015;98:507–17. https://doi.org/10.1111/cxo.12312.
8. Cameron MA, et al. Electroretinography of wild-type and Cry mutant mice reveals circadian tuning of photopic and mesopic retinal responses. J Biol Rhythms. 2008;23:489–501. https://doi.org/10.1177/0748730408325874.
9. Pardue MT, Stone RA, Iuvone PM. Investigating mechanisms of myopia in mice. Exp Eye Res. 2013;114:96–105. https://doi.org/10.1016/j.exer.2012.12.014.
10. Huang F, et al. Retinal dopamine D2 receptors participate in the development of myopia in mice. Invest Ophthalmol Vis Sci. 2022;63:24. https://doi.org/10.1167/iovs.63.1.24.
11. Jiang X, et al. Violet light suppresses lens-induced myopia via neuropsin (OPN5) in mice. Proc Natl Acad Sci U S A. 2021. https://doi.org/10.1073/pnas.2018840118.
12. Yang J, et al. A role of color vision in emmetropization in C57BL/6J mice. Sci Rep. 2020;10:14895. https://doi.org/10.1038/s41598-020-71806-0.
13. Veilleux CC, Kirk EC. Visual acuity in mammals: effects of eye size and ecology. Brain Behav Evol. 2014;83:43–53. https://doi.org/10.1159/000357830.

14. Wong AA, Brown RE. Visual detection, pattern discrimination and visual acuity in 14 strains of mice. Genes Brain Behav. 2006;5:389–403. https://doi.org/10.1111/j.1601-183X.2005.00173.x.
15. Tkatchenko TV, Shen Y, Tkatchenko AV. Mouse experimental myopia has features of primate myopia. Invest Ophthalmol Vis Sci. 2010;51:1297–303. https://doi.org/10.1167/iovs.09-4153.
16. Pardue MT, et al. High susceptibility to experimental myopia in a mouse model with a retinal on pathway defect. Invest Ophthalmol Vis Sci. 2008;49:706–12. https://doi.org/10.1167/iovs.07-0643.
17. Tkatchenko TV, et al. Photopic visual input is necessary for emmetropization in mice. Exp Eye Res. 2013;115:87–95. https://doi.org/10.1016/j.exer.2013.06.025.
18. Sze YH, et al. High-pH reversed-phase fractionated neural retina proteome of normal growing C57BL/6 mouse. Sci Data. 2021;8:27. https://doi.org/10.1038/s41597-021-00813-1.
19. Schmucker C, Schaeffel F. A paraxial schematic eye model for the growing C57BL/6 mouse. Vision Res. 2004;44:1857–67. https://doi.org/10.1016/j.visres.2004.03.011.
20. Jiang M, et al. Single-shot dimension measurements of the mouse eye using SD-OCT. Ophthalmic Surg Lasers Imaging. 2012;43:252–6. https://doi.org/10.3928/15428877-20120308-04.
21. Geng Y, et al. Optical properties of the mouse eye. Biomed Opt Express. 2011;2:717–38. https://doi.org/10.1364/BOE.2.000717.
22. Ashton JR, West JL, Badea CT. In vivo small animal micro-CT using nanoparticle contrast agents. Front Pharmacol. 2015;6:256. https://doi.org/10.3389/fphar.2015.00256.
23. Park H, et al. Assessment of axial length measurements in mouse eyes. Optom Vis Sci. 2012;89:296–303. https://doi.org/10.1097/OPX.0b013e31824529e5.
24. Tkatchenko TV, Shen Y, Tkatchenko AV. Analysis of postnatal eye development in the mouse with high-resolution small animal magnetic resonance imaging. Invest Ophthalmol Vis Sci. 2010;51:21–7. https://doi.org/10.1167/iovs.08-2767.
25. Drager UC, Olsen JF. Ganglion cell distribution in the retina of the mouse. Invest Ophthalmol Vis Sci. 1981;20:285–93.
26. Sterratt DC, Lyngholm D, Willshaw DJ, Thompson ID. Standard anatomical and visual space for the mouse retina: computational reconstruction and transformation of flattened retinae with the Retistruct package. PLoS Comput Biol. 2013;9: e1002921. https://doi.org/10.1371/journal.pcbi.1002921.
27. Hunt OA, Wolffsohn JS, Gilmartin B. Evaluation of the measurement of refractive error by the PowerRefractor: a remote, continuous and binocular measurement system of oculomotor function. Br J Ophthalmol. 2003;87:1504–8. https://doi.org/10.1136/bjo.87.12.1504.
28. Lou L, Hall KM, Pardue MT. Effect of OCT alignment on ocular parameters in the mouse eye. Invest Ophthalmol Vis Sci. 2023;64:847–847.
29. Perez-Merino P, et al. Three-dimensional OCT based guinea pig eye model: relating morphology and optics. Biomed Opt Express. 2017;8:2173–84. https://doi.org/10.1364/BOE.8.002173.
30. Batista A, et al. Normative mice retinal thickness: 16-month longitudinal characterization of wild-type mice and changes in a model of Alzheimer's disease. Front Aging Neurosci. 2023;15:1161847. https://doi.org/10.3389/fnagi.2023.1161847.

Publisher's Note